Journal of Advanced Ceramics
2024, **13**(10): 1622–1634
https://doi.org/10.26599/JAC.2024.9220962

Research Article

Synergistic promotion of dielectric and thermomechanical properties of porous Si_3N_4 ceramics by a dual-solvent template method

Yuanyuan Liu, Zhilin Tian✉, Liya Zheng, Bin Li✉

School of Materials, Shenzhen Campus of Sun Yat-sen University, Shenzhen 518107, China

Received: April 12, 2024; Revised: August 20, 2024; Accepted: August 26, 2024

Abstract: Porous Si_3N_4 ceramics are promising high-temperature wave transparent materials for use as radomes or antenna windows in hypersonic aircraft. However, a trade-off between the dielectric and thermomechanical properties is still challenging. Therefore, tailoring the microstructure and properties of porous Si_3N_4 is highly important. In this work, porous Si_3N_4 ceramics with uniform and fine structures were obtained via dual-solvent templating combined with the freeze-casting method. The as-prepared porous Si_3N_4 ceramic, with 56% porosity, possesses high mechanical properties, with flexural strength and compressive strength values of 95±14.8 and 132±4.5 MPa, respectively. The uniform spherical pore structure improved the mechanical properties, and the rod-shaped Si_3N_4 grains facilitated crack deflection. The decreased pore size effectively blocks phonon transport, leading to a low thermal conductivity of only 4.2 W/(K·m). Moreover, the porous Si_3N_4 ceramic maintains a small dielectric constant of 3.3, and the dielectric loss is stable between 1.0×10^{-3}–4.0×10^{-3}, which guarantees its potential application in high-temperature wave-transparent components. These results significantly advanced the development of high-performance wave-transparent materials used in hypersonic aircraft.

Keywords: Si_3N_4; porous ceramics; freeze-casting; wave-transparent material; dual solvent

1 Introduction

The radome and wave-transparent antenna window are key structural components in aircraft that protect the radar antenna from external interference while maintaining normal communication [1–3]. It is generally believed that if the material's dielectric constant is less than 10 and the dielectric loss is less than 1×10^{-2}, the material can obtain more ideal wave-transparent performance and aiming error. During high-speed flight, they are exposed to extremely harsh environments, including aerodynamic heating and impact loads [4]. Therefore, an ideal wave-transparent antenna window or radome material for hypersonic aircraft should possess high strength [5], a low dielectric constant [6], high thermal shock resistance [7], and good thermal insulation properties [4,8].

At present, the most widely used wave-transparent materials are mainly oxide- and nitride-based ceramics. These include SiO_2, BN, Si_3N_4, etc. [9,10]. The mechanical strength of SiO_2 and BN is low, and their load-bearing performance is poor [8,11]. The Si_3N_4 ceramic possesses a high melting point and excellent mechanical properties and is a potential wave-transparent material for hypersonic aircraft [12,13]. However, the dielectric properties and thermal insulation properties of dense Si_3N_4 ceramics need to be improved to meet the requirements of precision waveguides and thermal insulation protection during high-speed flight. The dielectric, mechanical, and thermal properties of wave-transparent materials can be improved by adjusting the microstructure, and porous ceramics provide a rich and diverse pore structure that offers multiple paths for intrinsic performance modulation [14–16]. However, increasing porosity is beneficial for improving the dielectric and thermal insulation properties but also significantly reduces the mechanical strength [17–19]. The dielectric constant of porous Si_3N_4 ceramics with porosities of 40%–55% can be reduced to 2.7–3.3 [13]. When the porosity of porous Si_3N_4 ceramics is greater than 35%, the flexural strength is lower than 100 MPa, making their application in a hypersonic flight environment difficult. The trade-off between the dielectric and mechanical properties faces serious challenges. Therefore, the modulation of the pore structure for synergistic enhancement of the dielectric and mechanical properties is important for the design of high-temperature wave-transparent materials [19].

Currently, there are many methods for preparing porous ceramics, such as the direct foaming method [20], gel molding method [21], and organic template impregnation method [22]. The direct foaming method is simple and can be used to prepare isotropic porous ceramics with high porosity. However, poor control of the foam results in uneven pore sizes and uncontrollable pore density [23,24]. The organic template impregnation method can obtain porous structures with uniform pore sizes, but larger pore sizes and incomplete removal of organic templates greatly affect the purity and performance of porous materials [23,25]. The freeze-drying method uses solvent crystals as sacrificial templates to prepare porous ceramics. Solvent crystals can be removed by sublimation at low pressure and temperature [25,26]. By retaining the ceramic matrix, porous materials with high porosity can be prepared. By changing factors such as the

✉ Corresponding authors.
E-mail: Z. Tian, tianzhlin@mail.sysu.edu.cn;
B. Li, libin75@mail.sysu.edu.cn

type of solvent and freezing rate, the freeze-drying method can yield different pore structures, achieve the modulation of material properties, and broaden the potential applications of porous materials [27]. The pore structures currently prepared by the freeze-drying method mainly include lamellar pores (using water as the solvent) [28], prismatic pores (using tert-butyl alcohol as the solvent) [29], and spherical pore structures (using camphene as the solvent) [30]. Only a few types of solvents can be used, as the solvent needs to present high vapor pressures, and the melting point of the solvent should be higher than the cooling temperature of a commercial freeze dryer. Multisolvent systems can propose new options to solve the problem of single-pore structures, which provides a new perspective on the microstructure regulation of porous ceramics [31]. At present, few studies have focused on the preparation of porous ceramic materials using multisolvent crystals as templates. Therefore, the use of multiple solvents as templates to prepare porous ceramics, which can control the pore structure through rational design of solvent systems and then synergistically improve the dielectric properties and mechanical properties, is necessary. To address this, a mixed solvent of tert-butyl alcohol and camphene was applied as a template, and the freeze-drying method was combined to synthesize porous Si_3N_4 ceramics in this work. This method allows for precise control over pore size and pore structure, which are crucial factors in the performance of high-temperature wave-transparent materials. Traditional methods such as direct foaming, gel casting, and organic template impregnation methods often fall short of achieving uniformity and regulation of the pore structure [20–26].

In this work, porous Si_3N_4 ceramics with uniform and fine structures were designed via a dual-solvent templating combined with freeze-casting method. The crystal growth process in mixed solvents was monitored to explain the various microstructures of the porous Si_3N_4 ceramics produced with different solvent compositions. The effect of the solvent ratio on the pore size distribution of the porous ceramics was analyzed, and the factors influencing the thermal, mechanical, and dielectric properties of the porous Si_3N_4 ceramics were investigated. The as-prepared porous Si_3N_4 ceramic presents uniformly distributed pores and a minimal pore size, endowing the material with excellent flexural and compressive strengths while improving its dielectric properties. The results of this work are expected to provide guidelines for the design of porous functional and structural ceramics.

2 Experimental

2.1 Material

α-Si_3N_4 powder was obtained from Xinjiang Jingshuo New Materials Company in China. Tert-butyl alcohol (99.99%, Macklin, China) and camphene (75%, Macklin, China) were used as templates. The polyvinyl butyral (PVB; MW, 25,000–40,000, Macklin, China) was utilized as the binder. MgO (AR, Aladdin, China) and Y_2O_3 (AR, China Rare Earth Resources and Technology Company, China) were employed as sintering aids.

2.2 Sample preparation

First, the volume ratios of tert-butyl alcohol and camphene were measured. The samples were defined as 1 : 0, 3 : 1, 2 : 1, 1 : 1, 1 : 2, 1 : 3, or 0 : 1 according to the ratio of the two solvents. Then, 20 vol% Si_3N_4 powder, 80 vol% solvent, 2 wt% MgO, 2 wt% Y_2O_3, and 2 wt% PVB were weighed. All the powders were added to the mixed solvent and ball milled together for 18 h to obtain Si_3N_4 slurry. The ceramic slurry was subsequently poured into a silicone mold (50 mm × 20 mm × 20 mm) and frozen in liquid nitrogen for 10 min. The frozen sample was dried in a freeze-dryer for 24 h to completely remove the solvent. Finally, the Si_3N_4 ceramic green body was annealed in a muffle furnace at 800 °C to remove carbon at a heating rate of 5 °C/min. Then, it was sintered at 1750 °C for 140 min in a nitrogen atmosphere to obtain the porous Si_3N_4 ceramic. The heating program was as follows: 8 °C/min to 1200 °C, then 5 °C/min to 1600 °C, and finally 3 °C/min to 1750 °C.

2.3 Characterizations

The microstructure was observed by a scanning electron microscope (SEM; TM4000, Hitachi, Japan), and high-resolution images were obtained via a transmission electron microscope (TEM; Talos F200X, Thermo Scientific, USA). The pore size and distribution of the porous Si_3N_4 ceramics were measured with a high-performance automatic mercury injection instrument (Auto Pore IV 9500, Micromeritics, USA). *In situ* observation of the growth process of solvent crystals under different solvent ratios was performed using inverted fluorescent crystals (BX22F-3M830F, AOSVI, China). The thermal conductivity was measured at room temperature via the planar heat source method (Auto Pore IV 9500, Micromeritics, USA). A three-dimensional X-ray microscope (μ-CT, Xradia 610, ZEISS, Germany) was used to obtain the three-dimensional pore structure. The flexural strength, compressive strength, and fracture toughness were obtained via an electronic universal testing machine (SNSS, C42.104, New Sansi, China). The loading speed was 0.5 mm/min. The dielectric properties of the porous ceramics were determined via the waveguide method in the X-band (12.4–18.0 GHz) via a vector network analyzer (PNA-N5244A, Agilent, USA). The dielectric constant at high temperatures (25–1100 °C, 7.0–18.0 GHz) was tested via the high-*Q* cavity method (HQR0718HT1150, Enchi Microwave, China).

3 Results and discussion

3.1 Microstructures of porous Si_3N_4 ceramics

The microstructures of the Si_3N_4 porous ceramics with different solvent ratios are shown in Figs. 1 and 2. When the solvent ratio is 1 : 0, the sample has an anisotropic prismatic pore structure. The pore structure changes significantly with increasing camphene volume. When the solvent ratio was 3 : 1, the pore structure was still prismatic. Unlike the sample with a 3 : 1 ratio, the pore structure of the sample with a 2 : 1 ratio is characterized by prism pores surrounded by spherical pores. However, when the volume ratio was 1 : 1, the prismatic pores disappeared, and the porous Si_3N_4 ceramic only exhibited spherical pores.

This phenomenon also appeared in samples with solvent ratios of 1 : 2, 1 : 3, and 0 : 1. The microstructures of the porous Si_3N_4 ceramics show that the dual-solvent system can increase the diversity of pore structures and that the pore structure is closely related to the solvent ratio. As the tert-butyl alcohol content decreases, the pore structure changes from prismatic to spherical.

TEM characterization provides high-resolution microstructural images that can display information such as the material's grain morphology, interface structure, and defect distribution. These factors may affect the thermal and mechanical properties of porous Si_3N_4 ceramics. SEM images of porous Si_3N_4 with different solvent ratios (Figs. 1 and 2) reveal that the porous Si_3N_4 ceramic with a solvent ratio of 1 : 2 has a uniformly distributed pore structure. Therefore, TEM characterizations of porous Si_3N_4

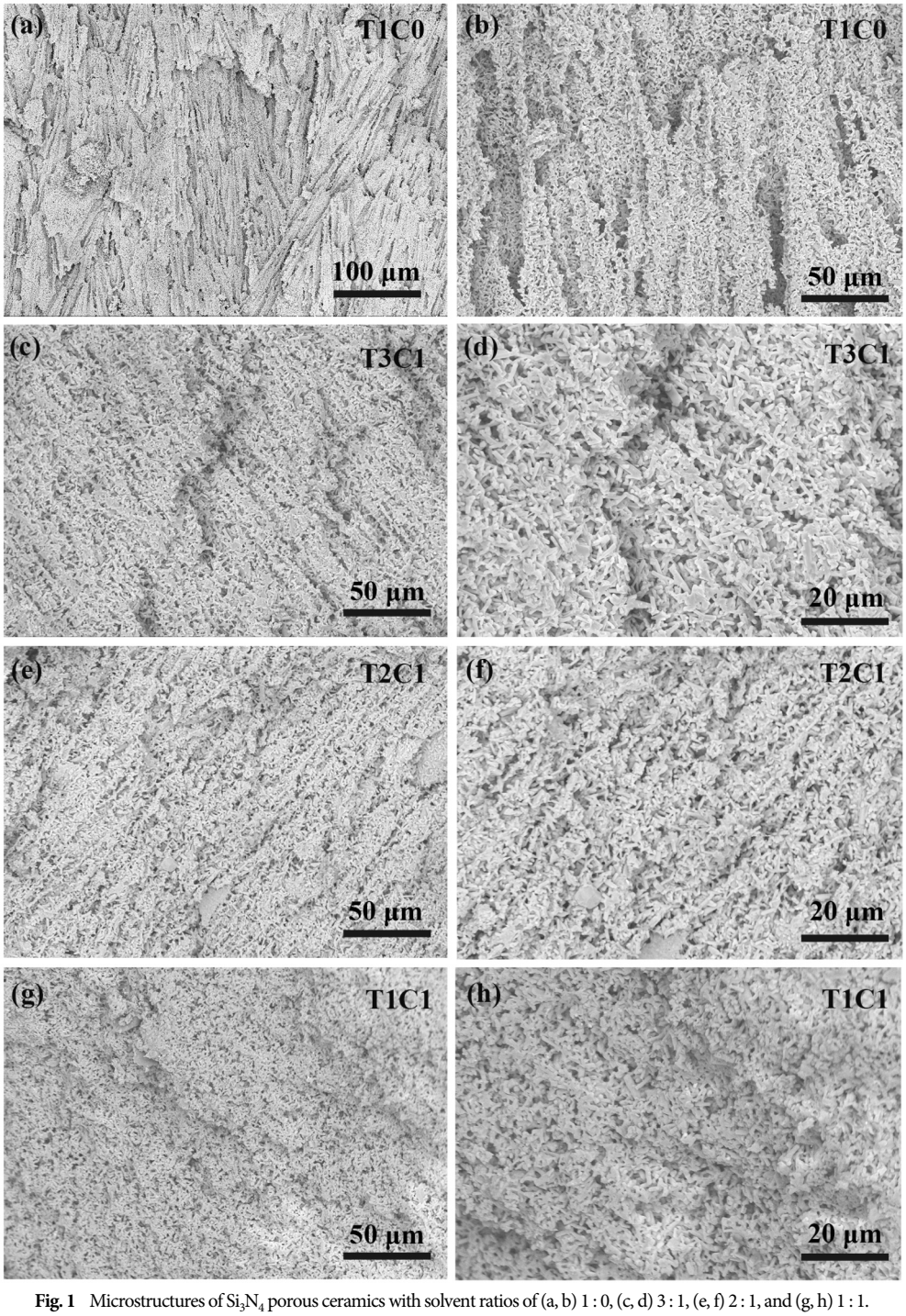

Fig. 1 Microstructures of Si_3N_4 porous ceramics with solvent ratios of (a, b) 1 : 0, (c, d) 3 : 1, (e, f) 2 : 1, and (g, h) 1 : 1.

ceramics with a solvent ratio of 1 : 2 were performed, and the results are shown in Fig. 3. Figure 3(a) shows that β-Si_3N_4 is a rod-shaped crystal with a length of approximately 4 μm. Figure 3(b) shows a high-resolution transmission electron microscopy (HRTEM) image of the boxed area in Fig. 3(a), in which the measured *d*-spacing of 0.66 nm is consistent with the (010) crystallographic plane of β-Si_3N_4. Figure 3(c) shows the corresponding electron diffraction image, which can be indexed as the [$\bar{1}$00] zone axis diffraction pattern of the β-Si_3N_4 crystal. The TEM image in Fig. 3(d) shows the grain boundary triple junction region. The results of the fast Fourier transform analysis, as shown in Fig. 3(e), indicate that the grain boundaries are composed of multiple phases. After performing the inverse fast Fourier transform in Fig. 3(e), lattice mismatch can be observed, as shown in Fig. 3(f). The elemental mapping of the grain boundary region is shown in Figs. 3(g), 3(h), 3(j)–3(l). The grain boundary area is rich in Mg, Y, and O, which is speculated to be the MgO–Y_2O_3 polycrystalline phase formed by MgO and Y_2O_3 sintering aids.

The pore size distribution was tested to clarify the changes in the pore structure of the Si_3N_4 ceramics. As shown in Fig. 4(a), the pore size distribution of the porous Si_3N_4 ceramics obtained with tert-butyl alcohol as the solvent is mainly in the range of 1–10 μm, with a bimodal distribution and two peaks corresponding to 1.60 and 6.58 μm. The pores measuring approximately 6 μm result from the sublimation of tert-butyl alcohol crystals, whereas the approximately 1 μm pores arise from the aggregation of rod-

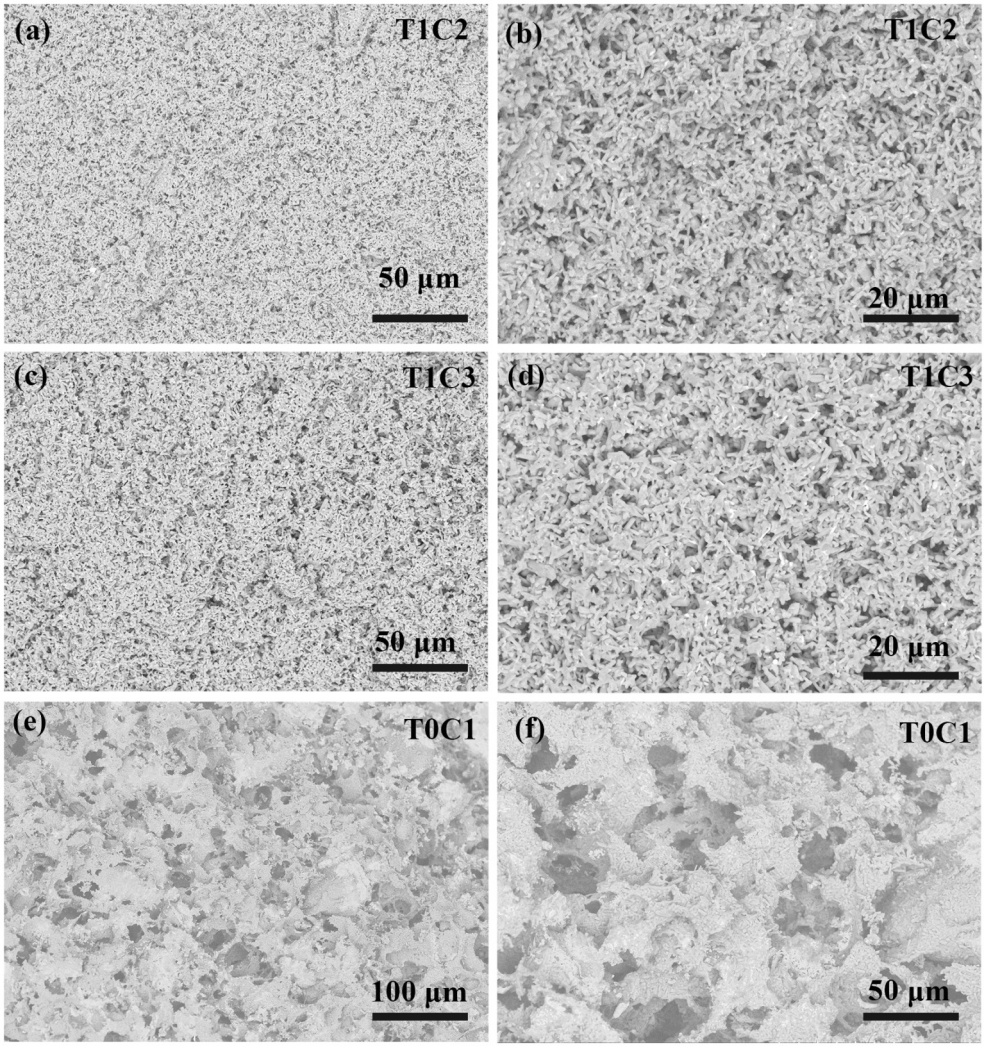

Fig. 2 Microstructures of porous Si_3N_4 ceramics with solvent ratios of (a, b) 1 : 2, (c, d) 1 : 3, and (e, f) 0 : 1.

shaped β-Si_3N_4 grains. When a mixture of 75 vol% tert-butyl alcohol and 25 vol% camphene was used as the solvent (Fig. 4(b)), the pore size distribution became narrow, and the pore size corresponding to the highest peak decreased to 2.04 μm. The pore sizes corresponding to the highest peak are 1.18 μm and 1.40 μm for samples 2 : 1 and 1 : 1, respectively, as shown in Figs. 4(c) and 4(d).

With decreasing tert-butyl alcohol content (1 : 2), the pore size distribution further narrows, and the pore size corresponding to the highest peak reaches a minimum value of only 0.74 μm. The content of tert-butyl alcohol continues to decrease, and the pore size corresponding to the highest peak begins to increase. The pore size distribution results show that the solvent ratio has a great influence on the pore size of Si_3N_4 ceramics. The relationship between the average pore size of the sample and the camphene content (Fig. 4(h)) reveals that as the camphene content increases, the pore size first decreases but then increases. In addition, the average pore size reached the minimum value when the solvent ratio was 1 : 2. This is related to the fact that the crystals of the two solvents compete with each other for growth space. When there is more tert-butyl alcohol with a larger crystal size, the pore size is larger. As the tert-butyl alcohol content decreases, smaller camphene crystals dominate the microstructure, and the pore size decreases.

Figure 5 shows the microstructure of the porous Si_3N_4 ceramics drawn via the software CINEMA 4D, showing the changes in pore structure and pore size with respect to the solvent ratio. The pore structure formed by the accumulation of rod-shaped β-Si_3N_4 particles gradually changes from prismatic to spherical. In particular, the solvent ratio of 1 : 1 becomes the dividing point for pore structure changes. When the solvent ratio was 3 : 1 or 2 : 1, the porous Si_3N_4 ceramic exhibited prismatic pores with shapes similar to those of tert-butyl alcohol crystals. When the solvent ratio was 1 : 1, 1 : 2, or 1 : 2, the porous Si_3N_4 ceramic exhibited spherical pores with shapes similar to those of camphene crystals. Notably, when the solvent ratio was 1 : 2, the porous Si_3N_4 ceramic exhibited the most uniform spherical pore structure with the smallest pore size.

The three-dimensional skeletons of porous ceramics with solvent ratios of 1 : 2, 1 : 0, and 0 : 1 were tested via X-ray computed tomography (CT). As shown in Fig. 6, the porous ceramics are composed of a Si_3N_4 ceramic skeleton and pores. The 3D images were analyzed to separate the skeleton (marked in gray) and pores (marked in yellow). Rod-shaped Si_3N_4 ceramic grains establish a connecting skeleton to form an overall structure. The pore structures of porous Si_3N_4 ceramics with different solvent ratios are different. As shown in Fig. 6(b), the pore structure of the sample with a solvent ratio of 1 : 2 consists of uniformly distributed spherical pores, and the ceramic skeleton structure is clear. The sample with a solvent ratio of 1 : 0 has an

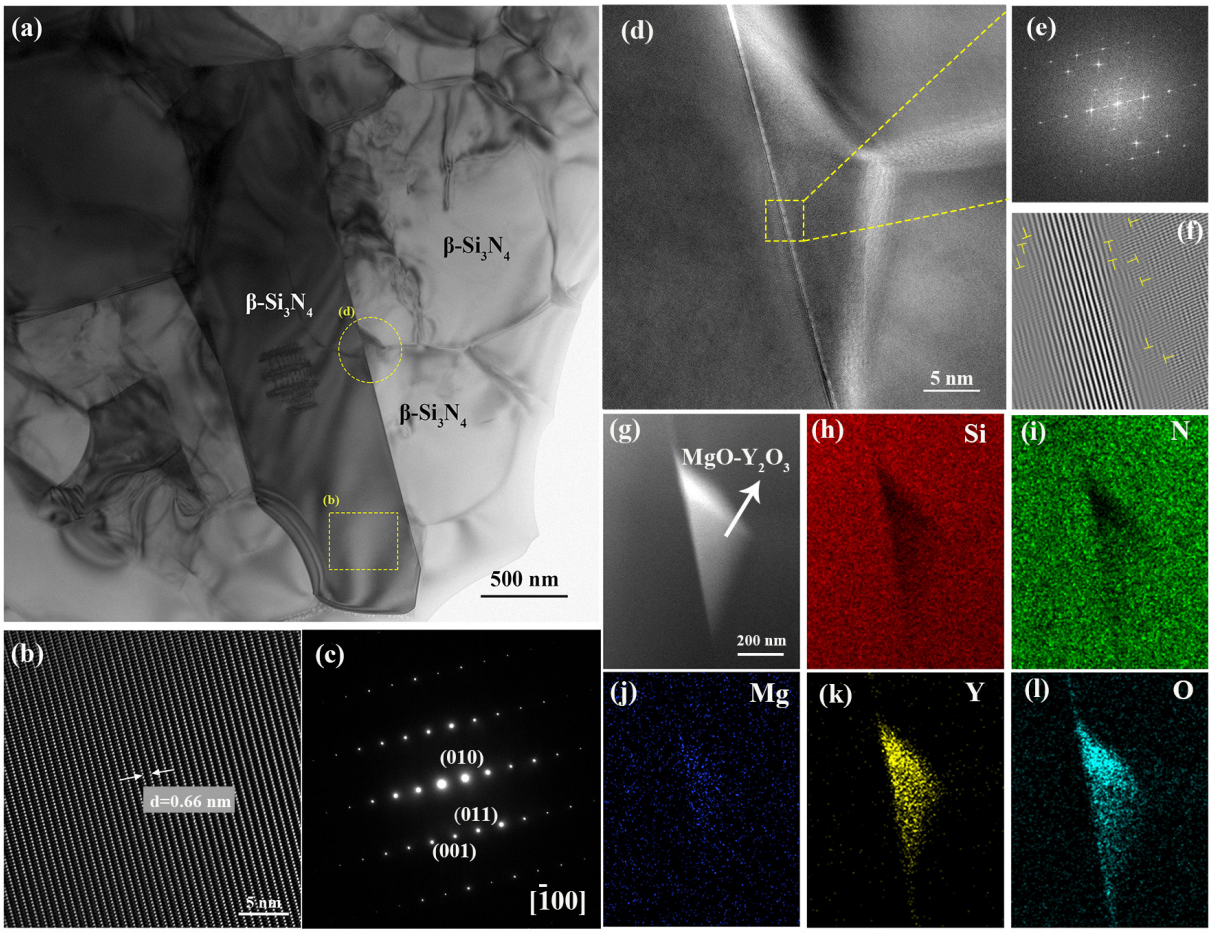

Fig. 3 Microstructures of porous Si_3N_4 ceramic with a solvent ratio of 1 : 2. (a) Low-magnification TEM images; (b) HRTEM images; (c) SAED of grain boundaries; (d) TEM images at grain boundaries; (e) fast Fourier transform (FFT) image and (f) inverse fast Fourier transform (IFFT) image of grain boundaries; (g) HADDF image and (h) Si, (i) N, (j) Mg, (k) Y, and (l) O distribution of triple junction.

anisotropic prismatic pore structure (Fig. 6(f)). When the solvent ratio was 0 : 1 (Fig. 6(j)), a spherical pore structure with uneven sizes and uneven pore distributions was observed. Figures 6(d), 6(h), and 6(l) show top–down perspective views of the cross section within the white box. The pore structure of the sample with a solvent ratio of 1 : 2 was spherical and uniform. When the solvent ratio was 1 : 0, both axial and transverse prism pores were present, indicating that the pores inside the sample were unevenly distributed. The sample 1 : 2 exhibited unique pore structure characteristics.

Porous Si_3N_4 was prepared via the freeze-drying method in this work. The sublimation of solvent crystals at low pressure will leave pores in the material. The morphology of the solvent crystals determines the structure of the pores. To explore the formation process of different pore structures, an inverted fluorescence microscope was used to observe the melting process of mixed solvent crystals with solvent ratios of 1 : 0, 0 : 1, and 1 : 2. Crystal crystallization and melting are opposite processes. The crystal melting process can be reversed to observe the crystallization process. The solvent was mixed with a small amount of fluorescent polystyrene microspheres and then crystallized by cooling with liquid nitrogen.

Figure 7(a) shows that tert-butyl alcohol first forms smaller elliptical crystals for approximately 0.65 s. Because tert-butyl alcohol crystals grow faster in the longitudinal direction, they eventually form prismatic crystals with lengths of approximately 500 μm and widths of approximately 100 μm. The growth process of the camphene crystals is shown in Fig. 7(b). The size of the first-formed spherical crystals gradually increases, and eventually, isotropic spherical crystals with a pore diameter of approximately 30 μm are formed. In particular, spherical crystals are directly connected. When 34 vol% tert-butyl alcohol and 66 vol% camphene are mixed (1 : 2), the solvent crystal growth process is completely different from the solvent crystal growth process at ratios of 1 : 0 and 0 : 1. As shown in Fig. 7(c), dispersed spherical crystals are formed first. As the freezing time increased, more spherical crystals formed to fill the gaps. Finally, spherical crystals with a pore size (~10 μm) much smaller than that of camphene crystals are obtained. The pore structure of porous Si_3N_4 ceramics is spherical because the melting point of camphene (~50 °C) is much greater than that of tert-butyl alcohol (~25 °C). During the cooling process, the camphene solidifies, forming small spherical crystals for approximately 0.58 s. They destroy the growth route of tert-butyl alcohol crystals, making it impossible to grow into large prismatic crystals.

3.2 Thermal properties of porous Si_3N_4 ceramic

The radome or antenna windows must possess good thermal resistance properties to maintain the normal operation of the antenna in harsh environments. The thermal conductivity of porous Si_3N_4 ceramics with solvent ratios of 1 : 0, 0 : 1, and 1 : 2 at room temperature was tested, as shown in Fig. 8(a). The thermal conductivity of the porous ceramics with a solvent ratio of 1 : 0 was the highest, and that with a ratio of 1 : 2 was the lowest. The

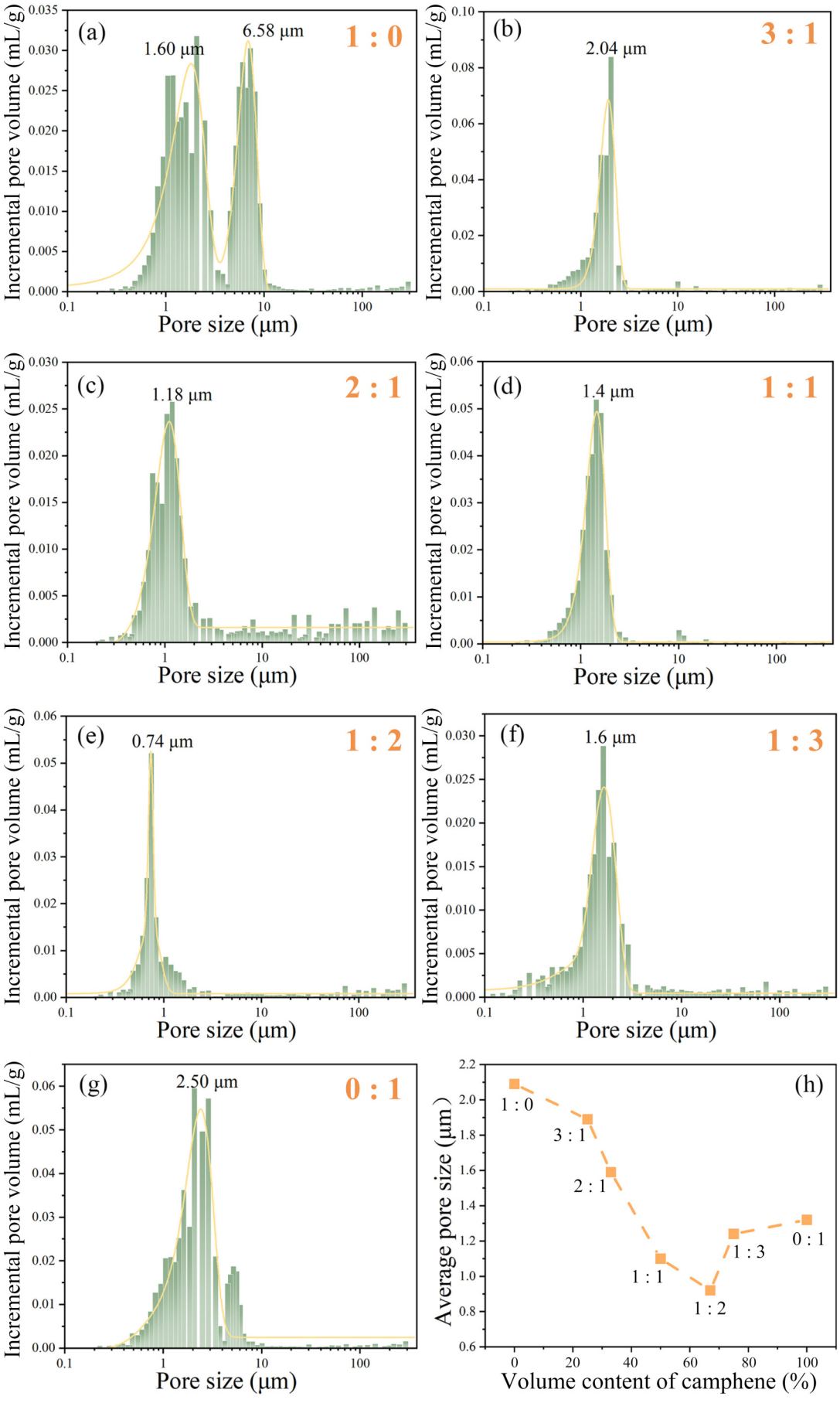

Fig. 4 Pore size distributions with (a) 1 : 0, (b) 3 : 1, (c) 2 : 1, (d) 1 : 1, (e) 1 : 2, (f) 1 : 3, and (g) 0 : 1 solvent ratios. (h) Average pore sizes of porous Si_3N_4 ceramics.

清華大学出版社 Tsinghua University Press | SciOpen

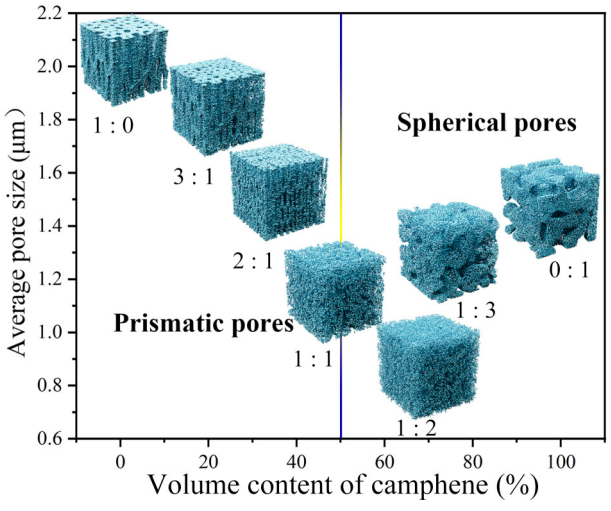

Fig. 5 Three-dimensional microstructures of porous Si_3N_4 ceramics prepared with different ratios of solvents used as templates.

thermal conductivity of the 1 : 2 sample is 4.2 W/(K·m), which is only 2/3 that of the 1 : 0 sample. This is strongly related to the pore structure of the porous material. As shown in Fig. 8(b), the pores of the porous Si_3N_4 ceramics with a solvent ratio of 1 : 0 are prismatic, and the heat transfer direction is parallel to the *c*-axis of the tert-butyl alcohol crystal. The heat is conducted mainly along the ceramic skeleton in the form of solid conduction, so the thermal conductivity is high. The porous Si_3N_4 ceramics obtained via the use of camphene crystals as templates have spherical pores, and the phonons are scattered at the gas-solid interface, which is conducive to reducing the thermal conductivity. The spherical pores of the porous Si_3N_4 ceramics with a solvent ratio of 1 : 2 are smaller and more evenly distributed.

Mercury porosimetry data show that porous ceramics with a solvent ratio of 1 : 2 have the largest total pore area (~0.894 m^2/g) and the smallest pore diameter, indicating that there are more gas-solid interfaces, thereby greatly enhancing phonon scattering. Therefore, the heat transfer path becomes more tortuous and complex, and the material presents a lower thermal conductivity [32].

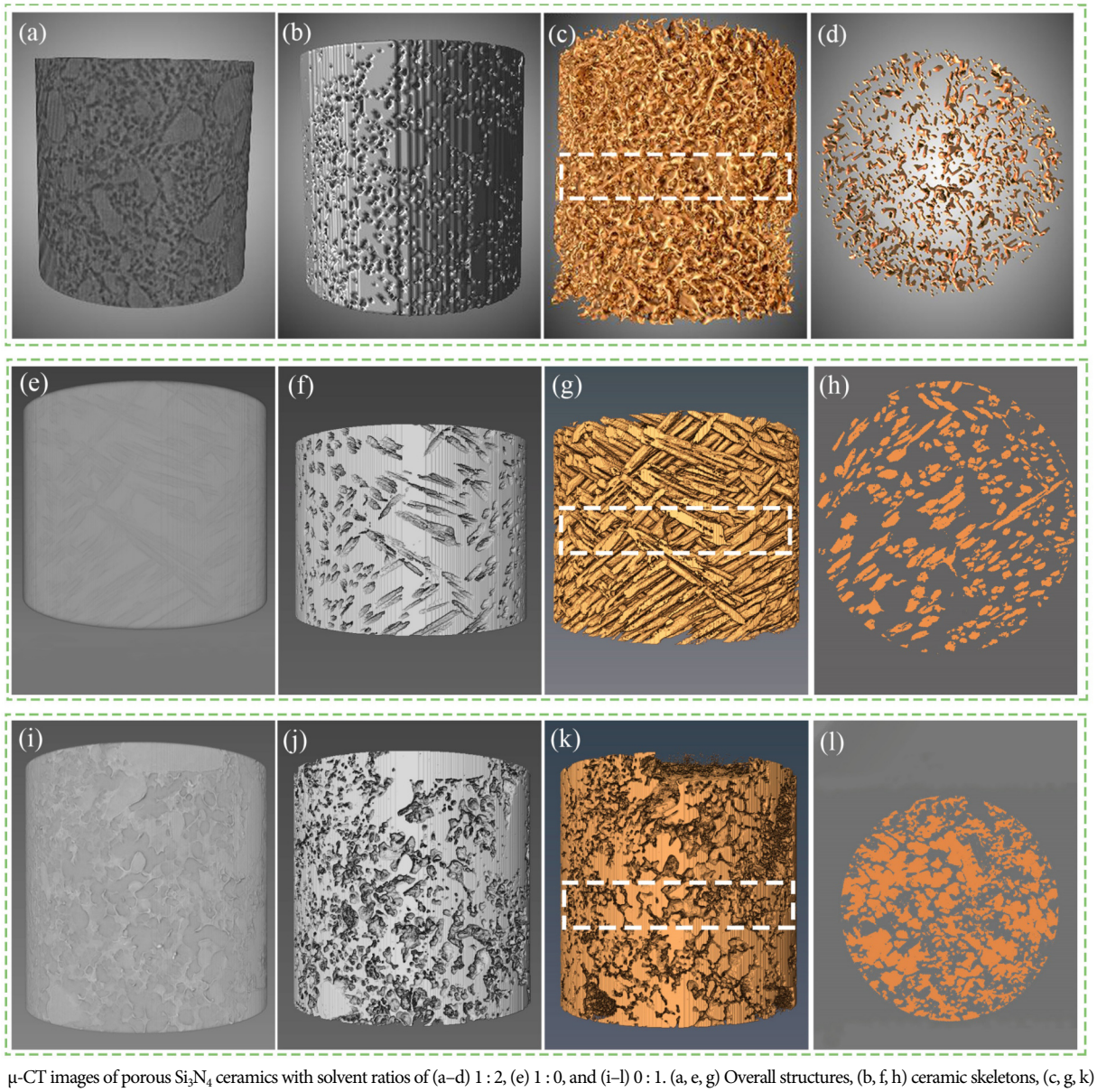

Fig. 6 μ-CT images of porous Si_3N_4 ceramics with solvent ratios of (a–d) 1 : 2, (e) 1 : 0, and (i–l) 0 : 1. (a, e, g) Overall structures, (b, f, h) ceramic skeletons, (c, g, k) pores, and (d, h, l) slices in white boxes of pores.

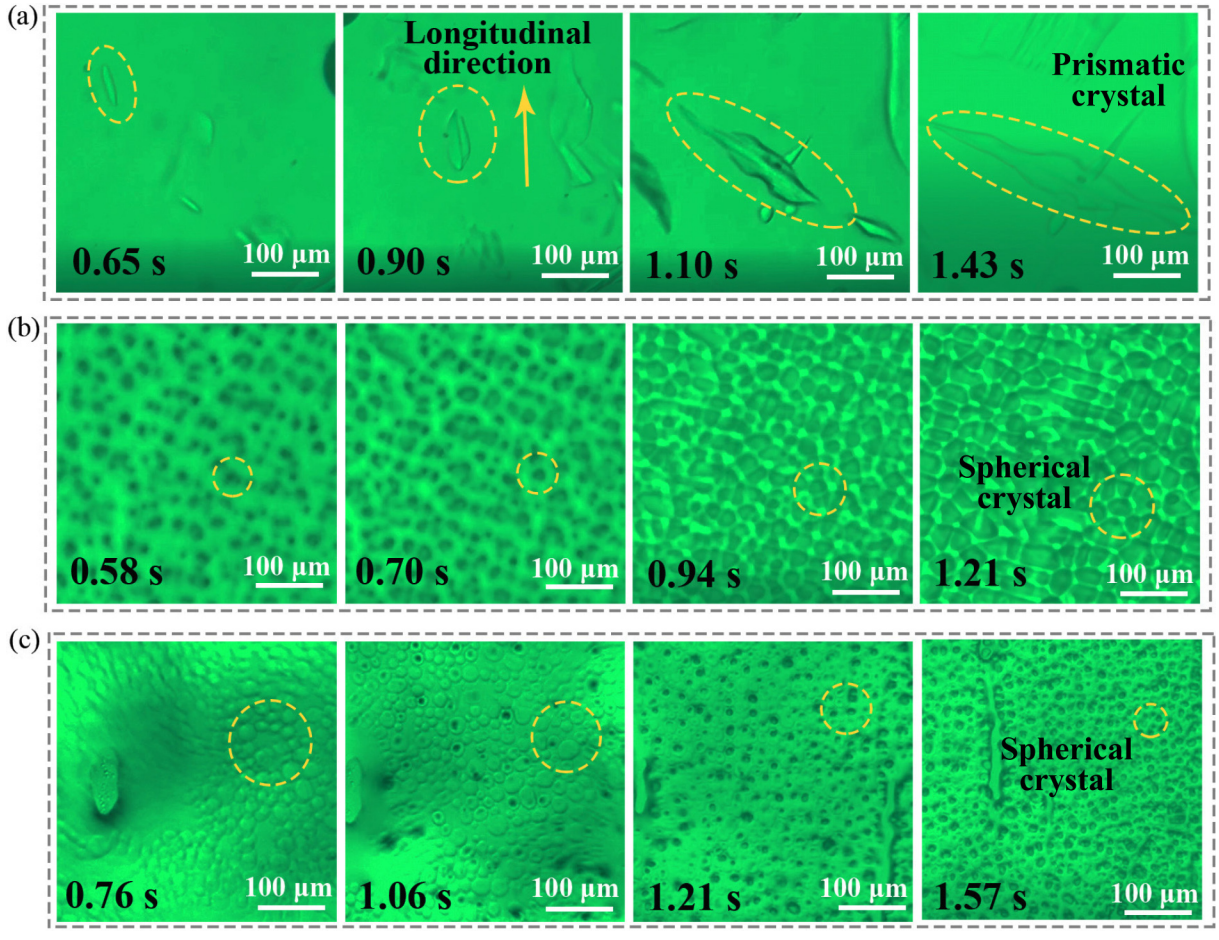

Fig. 7 *In situ* observation of solvent crystal growth process with (a) 1 : 0, (b) 0 : 1, and (c) 1 : 2 solvent ratios.

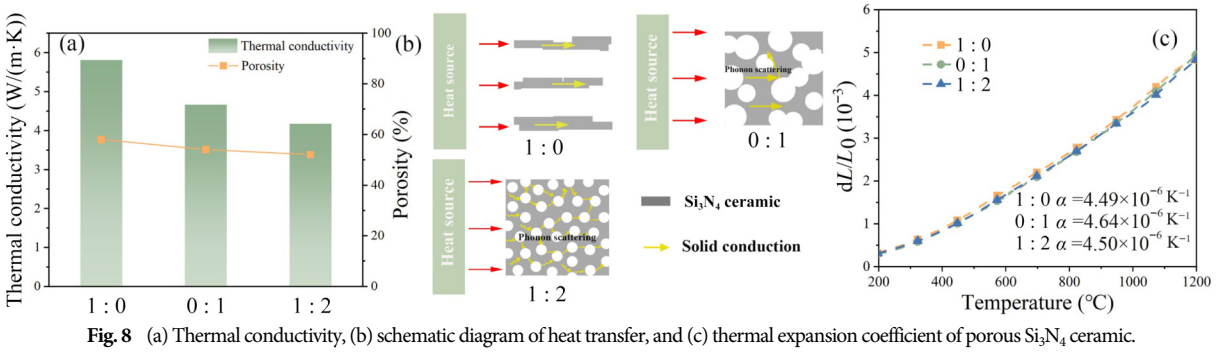

Fig. 8 (a) Thermal conductivity, (b) schematic diagram of heat transfer, and (c) thermal expansion coefficient of porous Si_3N_4 ceramic.

Furthermore, the TEM image (Fig. 3) shows that MgO and Y_2O_3 form a glassy phase between rod-shaped β-Si_3N_4 grains. This glass phase fills the gaps between the grains. The thermal conductivity of the glass phase is usually lower than that of the grains themselves, creating thermal resistance within the material and helping to improve the thermal properties of porous ceramics [33].

On the other hand, radomes or antenna windows are often subjected to sudden temperature changes, so they must be able to withstand thermal shock and avoid catastrophic damage [34]. A low thermal expansion coefficient is required to minimize the drastic degradation of materials [35]. The thermal expansion of the porous ceramics with the three solvent ratios is shown in Fig. 8(c). From 200 to 1200 °C, the length changes of the porous Si_3N_4 ceramics with solvent ratios of 1 : 0, 0 : 1, and 1 : 2 increase as the temperature increases, with an order of magnitude of 10^{-3}, and the change is small. This is due to the stability, anisotropy, and pore structure of Si_3N_4 grains, which can absorb thermal vibrations. The average coefficients of thermal expansion of samples 1 : 0, 0 : 1, and 1 : 2 are 4.49×10^{-6}, 4.64×10^{-6}, and 4.50×10^{-6} K^{-1}, respectively, from 200 to 1200 °C. The difference in the thermal expansion coefficients of these three samples is small because the pore structure inside the porous Si_3N_4 ceramic provides sufficient space for the thermal expansion of the ceramic matrix.

3.3 Mechanical properties of porous Si_3N_4 ceramics

The mechanical properties of the porous Si_3N_4 ceramics are depicted in Fig. 9. When the solvent ratio was 1 : 0, the flexural strength of the porous Si_3N_4 ceramics was less than 20 MPa. As the porosities of the porous Si_3N_4 ceramics with different solvent ratios are similar, the flexural strength is related mainly to the pore structure. The SEM image with a solvent ratio of 1 : 0 (Fig. 2) shows that the prismatic channels overlap with each other to form

channels with larger pore diameters. During the loading process, these large pores can be regarded as defects and have poor load-bearing capacity, thus resulting in a lower strength of the porous Si_3N_4 ceramic. When the solvent ratio was adjusted to 3 : 1, the flexural strength of the porous Si_3N_4 ceramics more than doubled compared with that of the sample with a ratio of 1 : 0. This improvement is attributed to the reduced width of the pores. When the solvent ratio is 2 : 1, the prismatic pores are more evenly distributed, and the overlap between pore channels is reduced, so the strength is further improved. The flexural strength of the 1 : 1 sample with a spherical pore structure is further increased because the spherical pores are more conducive to dispersing forces. At a solvent ratio of 1 : 2, its flexural strength reaches the maximum value of approximately 110 MPa. The pore structure is more uniform, and the sizes are smaller, resulting in greater strength. However, as the camphene volume content continues to increase (solvent ratios of 1 : 3 and 0 : 1), the flexural strength decreases. This is related to the unevenly distributed pore structure of the porous Si_3N_4 ceramics. As shown in Fig. 5, the pore size distribution of the porous Si_3N_4 ceramics with solvent ratios of 1 : 3 and 0 : 1 becomes wider, which means that the size and distribution of the pores become uneven. Larger pores and uneven distributions can lead to stress concentrations, increasing the susceptibility of the material to fracture and damage when stressed. It may even be concentrated in certain areas, causing localized brittle cracking or damage. The compressive strength is another important property to consider. The trend of the compressive strength is consistent with that of the flexural strength, as shown in Fig. 9(b). With increasing camphene content, the compressive strength first increases but then decreases. In addition, the compressive strength reached a maximum value of ~145 MPa when the solvent ratio was 1 : 2.

To gain a deeper understanding of the fracture process of the material, digital image correlation (DIC) technology was used to characterize the strain during the loading process of the modified material. As shown in Fig. 10(a), during the loading process, the strain in the middle of the sample gradually increased, indicating that the tensile stress on the sample gradually increased until the sample broke. In addition, the strain of the sample varies greatly near the left span. This may be because there are small cracks in the sample, so the small cracks gradually increase during the loading process. Figure 10(b) shows the three-dimensional strain distribution in the loading direction (*xx* direction). The strain is concentrated in the middle of the sample, indicating that this region is subjected to the greatest tensile stress. Figure 10(c) shows the transverse strain distribution perpendicular to the loading

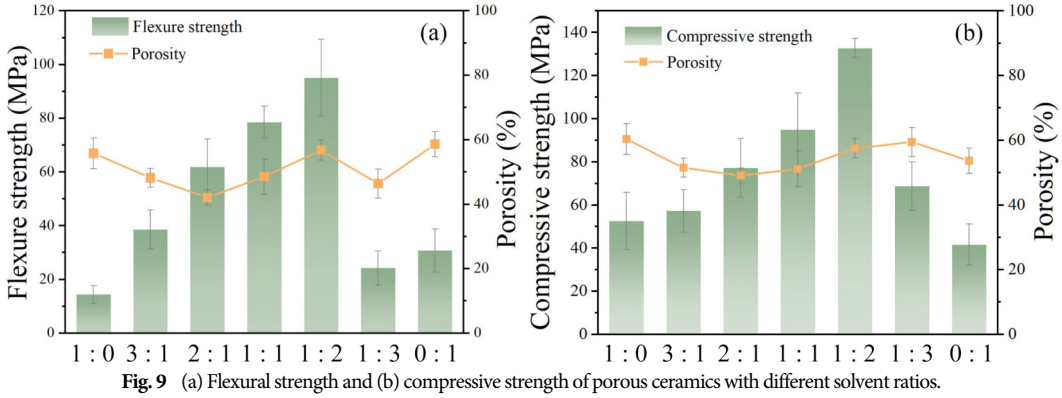

Fig. 9 (a) Flexural strength and (b) compressive strength of porous ceramics with different solvent ratios.

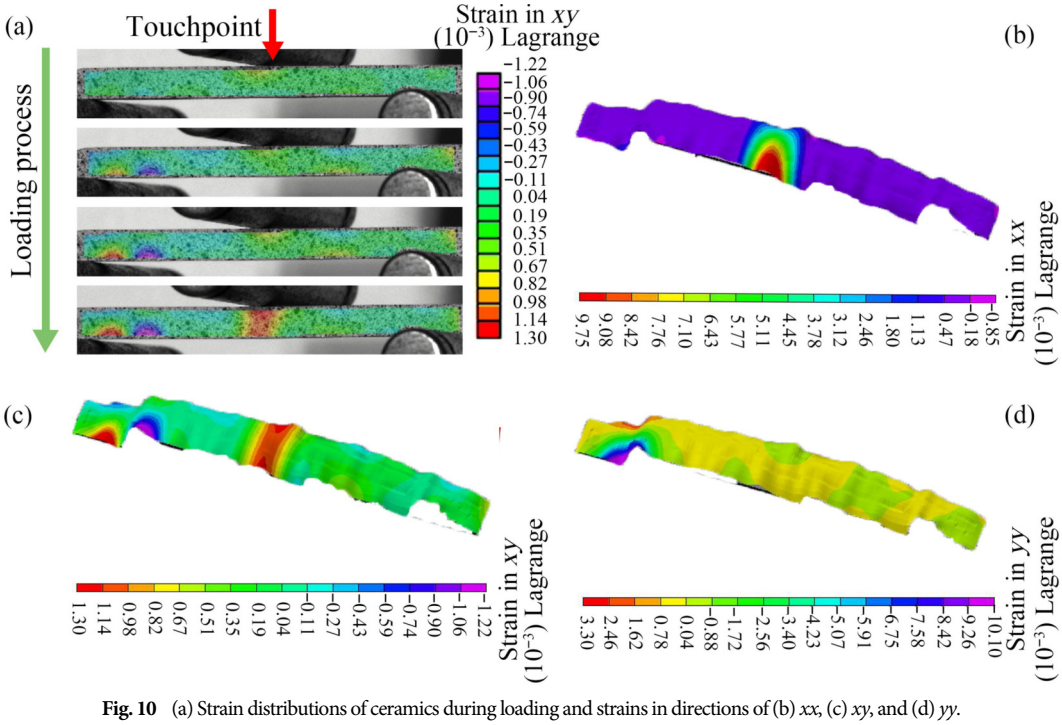

Fig. 10 (a) Strain distributions of ceramics during loading and strains in directions of (b) *xx*, (c) *xy*, and (d) *yy*.

direction (*xy* direction). The strain concentration is more obvious near the loading point. Figure 10(d) shows the strain distribution in the thickness direction (*yy* direction). The figure shows the strain gradient in the direction of the sample thickness. The strain distribution in the middle of the sample is relatively uniform, whereas the strain distribution near the left edge is not uniform. This may be related to edge effects and sample geometry.

Figure 11 depicts the fracture toughness and crack propagation of samples 1 : 0 and 1 : 2. The fracture toughness values of the porous Si_3N_4 ceramics with solvent ratios of 1 : 0 and 1 : 2 are 0.84±0.09 and 1.16±0.42 MPa·m$^{1/2}$, respectively. Figures 11(b) and 11(e) show that, owing to the different pore structures, the number and angle of crack deflection also differ. The 1 : 0 sample has wider cracks, fewer deflections, and smaller deflection angles. In contrast, in the 1 : 2 sample, the crack deflected multiple times during the propagation process. Greater crack deflection increases energy dissipation during crack propagation, which is beneficial for improving fracture toughness [36]. On the other hand, the 1 : 2 sample presents narrower cracks and larger deflection angles. The more twisted the crack path is, the more energy the sample absorbs during crack propagation. Figures 11(c) and 11(f) show SEM images of crack deflection in the porous ceramic section. The crack propagation path of the porous Si_3N_4 ceramics with a 1 : 2 solvent ratio was more tortuous than that of the samples with a 1 : 0 solvent ratio. In addition, rod-like Si_3N_4 grains are pulled out near the fracture, and elongated grains are more conducive to crack deflection [37].

Figures 12(a) and 12(b) present the two-dimensional and three-dimensional strain distributions of the porous Si_3N_4 ceramics on the *xy* plane during the fracture toughness test, respectively. In Fig. 12(a), as loading continues, the strain at the crack tip gradually increases, indicating that this area is subjected to significant tensile stress. This shows that during the loading process, tensile stress gradually accumulates and eventually leads to the fracture of the sample. The three-dimensional strain distribution shows that the strain is concentrated at the crack tip,

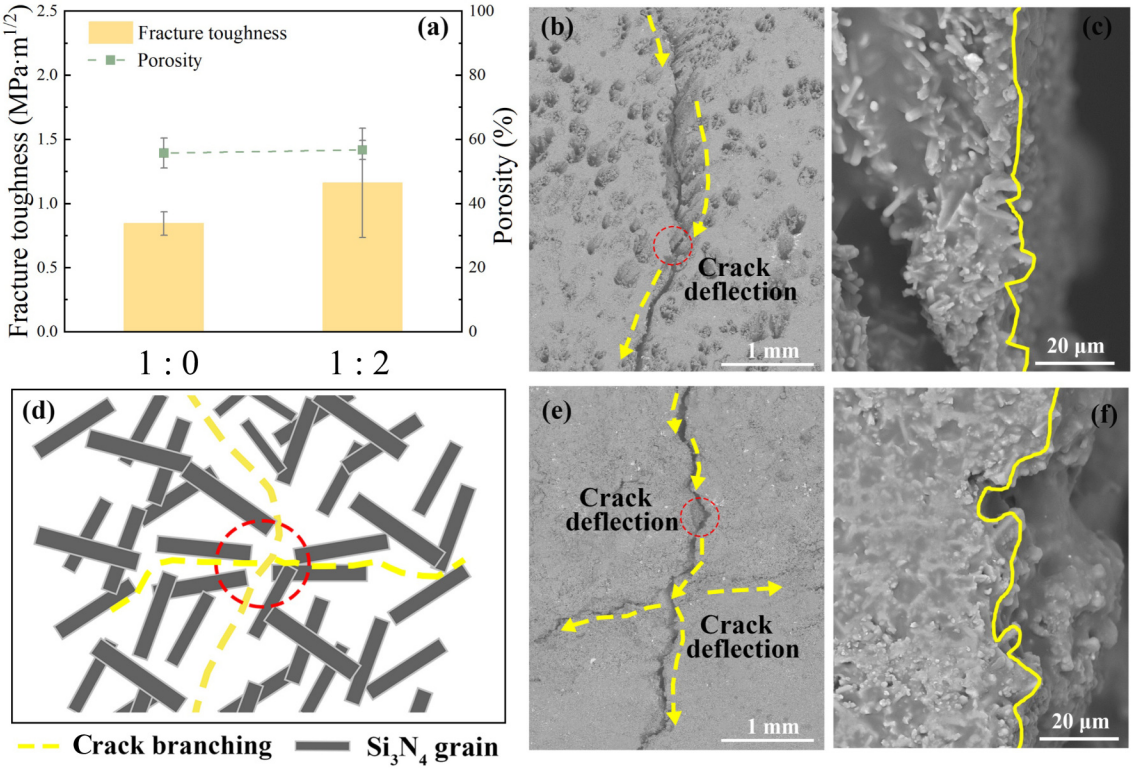

Fig. 11 (a) Fracture toughness of porous Si_3N_4 ceramics, (b) surface and (c) cross-sectional SEM image of crack growth for sample with 1 : 0 solvent ratio, (d) crack deflection diagram, (e) surface and (f) cross-sectional SEM image of crack growth for a sample with 1 : 2 solvent ratio.

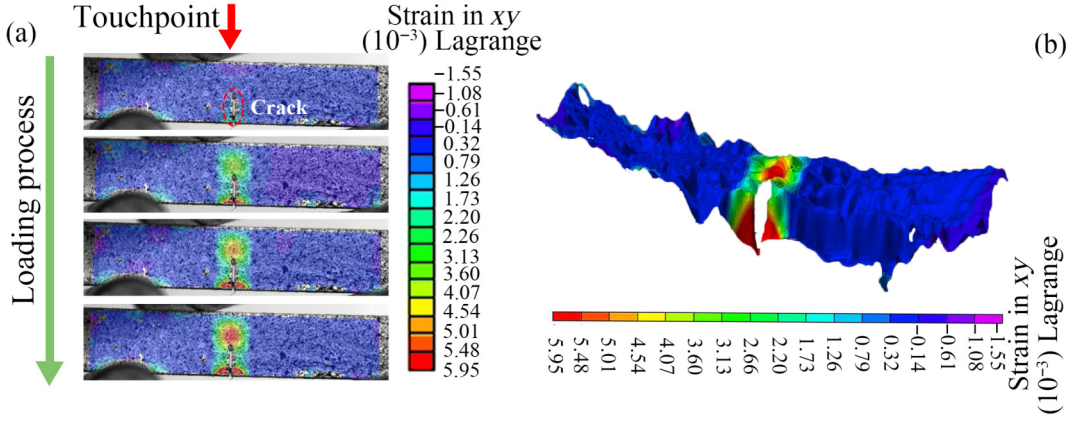

Fig. 12 (a) 2D and (b) 3D *xy* direction strain distributions during fracture toughness testing.

indicating that this area is subject to the maximum tensile stress. An obvious strain gradient can be seen in the strain distribution diagram, which gradually decreases outward from the crack, indicating the transfer and diffusion of stress concentration in the sample.

3.4 Dielectric properties of porous Si_3N_4 ceramics

The radome or antenna window materials used in aircraft require a low dielectric constant and dielectric loss to ensure precise guidance and communication. The waveguide method was used to test the dielectric constant of samples 1 : 0, 0 : 1, and 1 : 2 at room temperature (25 °C). As shown in Fig. 13(a), the dielectric constant of the three samples is stable at 3.3–3.7 in the range of 12.4–18.0 GHz. The porous Si_3N_4 ceramic with a solvent ratio of 1 : 2 presented the smallest dielectric constant, at only 3.3. The dielectric constant is influenced primarily by the molecular structure, chemical composition, and electron cloud polarization. The pore structure has a small effect on the dielectric constant [38]. The dielectric loss of the three samples is distributed between 1.0×10^{-3}–4.0×10^{-3}. The dielectric loss of the three samples at room temperature increases with increasing frequency, as shown in Fig. 13(b). This is related to the fact that the inertial effect of electrons becomes more significant at high frequencies, and electrons produce hysteresis when the electric field changes [39]. On the other hand, the interface between pores and the ceramic skeleton may lead to additional polarization effects [40]. The porous Si_3N_4 ceramic with a solvent ratio of 1 : 2 has more interfaces per unit volume. As the frequency increases, the polarization behavior of the interface becomes more significant, and the dielectric loss increases. Moreover, the stability of the dielectric properties at high temperatures is particularly important, and the high-Q cavity method is applied to evaluate the dielectric properties.

Figure 14 shows the relationship between the temperature-dependent dielectric constant and dielectric loss of the porous Si_3N_4 ceramic. As shown in Fig. 14(a), the dielectric constant of the porous Si_3N_4 ceramics is stable between 5.0 and 5.5 from room temperature to 1100 °C. However, the dielectric constant increases slightly at 900 °C and decreases again above 1000 °C. The dielectric constant does not change significantly as the temperature increases. On the other hand, because of the excellent electrical insulation of porous Si_3N_4 ceramics [41], the loss tangent of the 1 : 2 sample is lower than 6.0×10^{-3} and is almost independent of frequency and temperature. This finding indicates that the porous Si_3N_4 ceramics fabricated using tert-butyl alcohol-camphene as the solvent at a volume ratio of 1 : 2 are promising high-temperature transparent materials. The following formulas are commonly used to describe the temperature dependence of the dielectric constant and loss tangent [42].

$$\kappa = \frac{1}{\varphi}\cdot\frac{\Delta\varphi}{\Delta T} \tag{1}$$

where κ is the temperature coefficient, T is the temperature, and φ is the dielectric constant or loss tangent. According to Eq. (1), the temperature coefficients of the dielectric constant and loss tangent of the Si_3N_4 porous ceramics remain at approximately

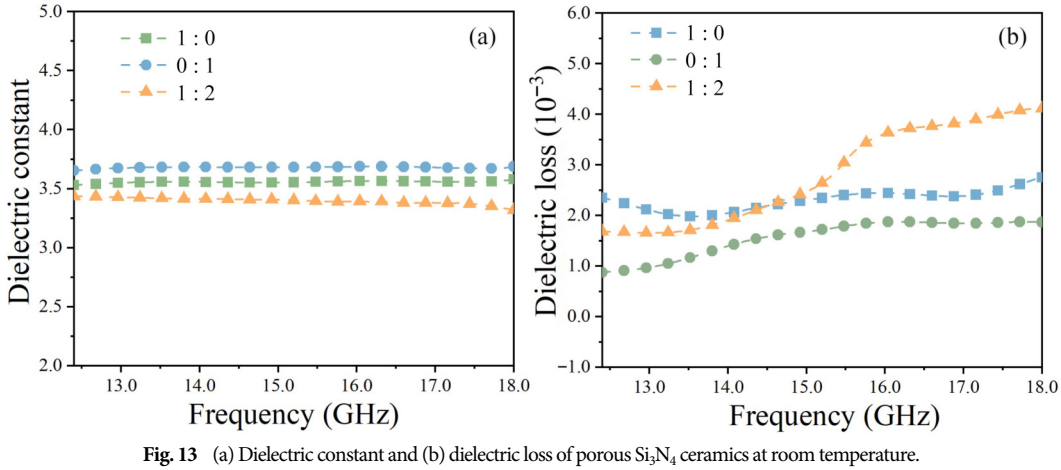

Fig. 13 (a) Dielectric constant and (b) dielectric loss of porous Si_3N_4 ceramics at room temperature.

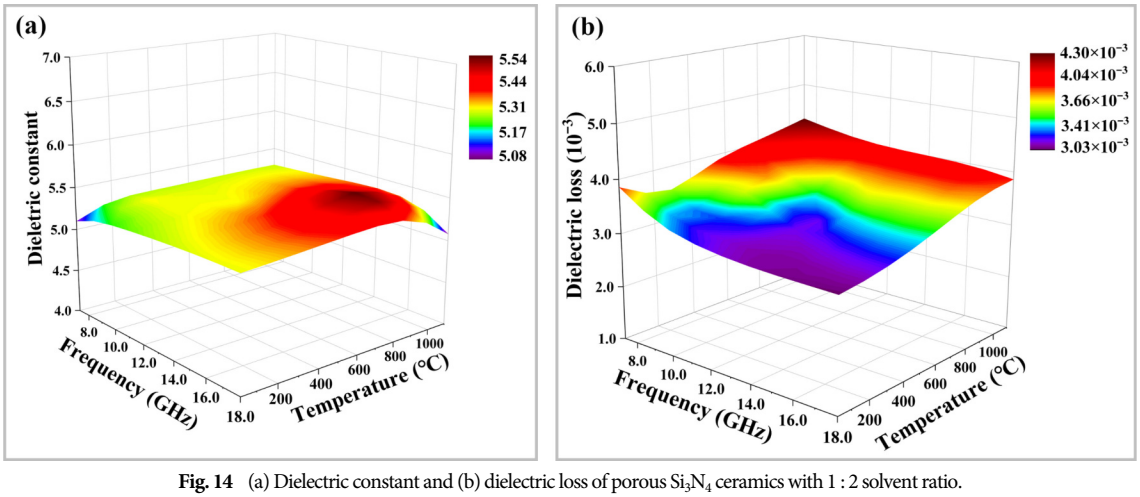

Fig. 14 (a) Dielectric constant and (b) dielectric loss of porous Si_3N_4 ceramics with 1 : 2 solvent ratio.

10^{-6} K^{-1} from room temperature to 1100 °C. This shows that the prepared Si_3N_4 ceramic has a weak temperature dependence and exhibits excellent thermal stability in terms of its dielectric response. The results in Figs. 12 and 13 indicate that there are differences in the dielectric constants of the porous Si_3N_4 ceramics. This difference may originate from the differences in measurement principles and application ranges between the waveguide method and the high-*Q* cavity method. Specifically, the waveguide method has a wide frequency range and can provide the dielectric properties of materials at different frequencies. However, it is affected by factors such as sample size and waveguide loss. The high-*Q* cavity method is generally considered to be more accurate at a single frequency point because of its high precision and high stability.

Figure 15 summarizes the porosity, flexural strength, and dielectric constant (the waveguide method) of the porous Si_3N_4 ceramics prepared in this work and other methods. Porous Si_3N_4 ceramics prepared using a dual solvent as a template present a lower dielectric constant and higher flexural strength than those prepared via pore-forming [43–45,48], inkjet printing [6], polymerization–pyrolysis [46], and gel-casting [12,47]. Compared with the porous Si_3N_4 ceramic prepared via the freeze–drying method [49–51] with a single solvent as a template, the 1 : 2 sample exhibited better dielectric properties and mechanical strength. The synergistic promotion of the dielectric constant and mechanical strength makes it a potential wave-transparent material in the aerospace industry.

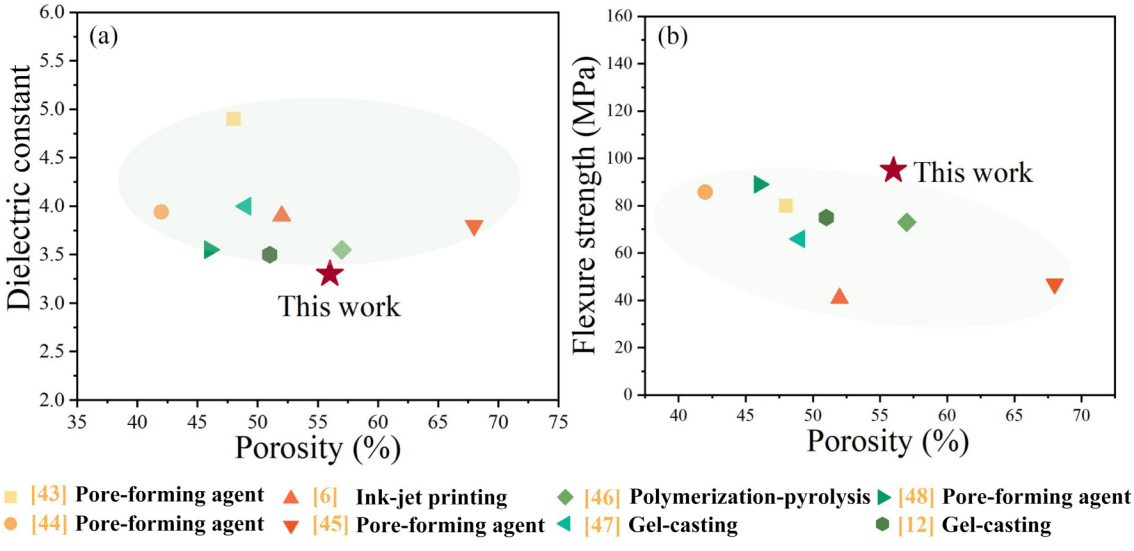

Fig. 15 Summary of (a) dielectric constant and (b) flexural strength of porous Si_3N_4-based ceramics prepared via different methods.

4 Conclusions

In this work, porous Si_3N_4 ceramics were prepared via freeze-drying using tert-butyl alcohol-camphene dual solvent crystals as templates. The shape and size of the pores can be effectively controlled and changed by adjusting the volume content of tert-butyl alcohol and camphene. With decreasing amounts of tert-butyl alcohol, the pore shape gradually changed from prismatic pores to spherical pores. On the other hand, the pore size first decreases and then increases, and when the volume ratio is 1 : 2, the pores of the porous Si_3N_4 ceramics are the most uniform and smallest. This structure endows the porous Si_3N_4 ceramic with excellent thermal insulation properties due to increased phonon scattering. Furthermore, the uniform pore structure enables the porous Si_3N_4 ceramics to exhibit excellent flexural strength and compressive strength. In addition, rod-shaped Si_3N_4 grains are conducive to crack deflection and greatly increase the fracture toughness of the material. The porous Si_3N_4 ceramic presents a low and stable dielectric constant and dielectric loss at high temperatures. Owing to these excellent properties, the freeze-casting method using dual solvent crystals as templates is expected to become a very promising method for preparing aerospace wave-transparent materials.

Acknowledgements

This work was financially supported by the National Natural Science Foundation of China (Grant No. 52202078), the Leading Talent Project of the National Special Support Program (Grant No. 2022WRLJ003), the Guangdong Basic and Applied Basic Research Foundation for Distinguished Young Scholars (Grant No. 2021B1515020083), and the Guangdong Basic and Applied Basic Research Foundation (Grant Nos. 2021A1515110293 and 2022A1515012201).

Declaration of competing interest

The authors have no competing interests to declare that are relevant to the content of this article.

References

[1] Xiong SX, Yang Y, Zhang SZ, *et al.* Nanoporous polybenzoxazine aerogels for thermally insulating and self-extinguishing materials in aerospace applications. *ACS Appl Nano Mater* 2021, **4**: 7280–7288.

[2] Barrios M, Van Sciver SW. Thermal conductivity of rigid foam insulations for aerospace vehicles. *Cryogenics* 2013, **55**: 12–19.

[3] Sundén B, Fu J. *Heat Transfer in Aerospace Applications*. Academic Press, 2016.

[4] Luo XY, Zhang Q, Ye F, *et al.* Microstructure, mechanical, wave-transparent and heat insulation properties of Si_3N_4 foam ceramic by organic foam impregnation combined with CVI. *J Mater Res Technol* 2023, **23**: 1332–1346.

[5] Yang XJ, Li B, Li D, *et al.* High-temperature properties and interface evolution of silicon nitride fiber reinforced silica matrix wave-transparent composite materials. *J Eur Ceram Soc* 2019, **39**: 240–248.

[6] Cheng ZL, Ye F, Liu YS, *et al.* Mechanical and dielectric properties of

porous and wave-transparent Si_3N_4–Si_3N_4 composite ceramics fabricated by 3D printing combined with chemical vapor infiltration. *J Adv Ceram* 2019, **8**: 399–407.
[7] Zhang RB, Fang DN, Chen XM, *et al.* Effect of pre-oxidation on the microstructure, mechanical and dielectric properties of highly porous silicon nitride ceramics. *Ceram Int* 2012, **38**: 6021–6026.
[8] Ye J, Zhang B, Zhang HQ, *et al.* Tuning the dielectric properties of porous BN/Si_3N_4 composites by controlling porosity. *J Eur Ceram Soc* 2023, **43**: 370–377.
[9] Xu Y, Jing Z, Gao YY, *et al.* Application of porous silicon nitride ceramics as cover material. *J Adv Ceram* 2022, **43**: 103–109.
[10] Chen SL, Wang L, He G, *et al.* Microstructure and properties of porous Si_3N_4 ceramics by gelcasting-self-propagating high-temperature synthesis (SHS). *J Adv Ceram* 2022, **11**: 172–183.
[11] Kenion T, Yang N, Xu CY. Dielectric and mechanical properties of hypersonic radome materials and metamaterial design: A review. *J Eur Ceram Soc* 2022, **42**: 1–17.
[12] Yang XJ, Li B, Zhang CR, *et al.* Fabrication and properties of porous silicon nitride wave-transparent ceramics via gel-casting and pressureless sintering. *Mater Sci Eng A* 2016, **663**: 174–180.
[13] Alem A, Pugh MD, Drew RAL. Open-cell reaction bonded silicon nitride foams: Fabrication and characterization. *J Eur Ceram Soc* 2014, **34**: 599–609.
[14] Su L, Li MZ, Wang HJ, *et al.* Resilient Si_3N_4 nanobelt aerogel as fire-resistant and electromagnetic wave-transparent thermal insulator. *ACS Appl Mater Interfaces* 2019, **11**: 15795–15803.
[15] Kawai C, Yamakawa A. Effect of porosity and microstructure on the strength of Si_3N_4: Designed microstructure for high strength, high thermal shock resistance, and facile machining. *J Am Ceram Soc* 1997, **80**: 2705–2708.
[16] Dai YJ, Hubálková J, Voigt C, *et al.* Tensile strength and damage of open-cell ceramic foams under cylindrical splitting test. *J Adv Ceram* 2023, **12**: 2003–2016.
[17] Tang LP. A study of the quantitative relationship between strength and pore-size distribution of porous materials. *Cem Concr Res* 1986, **16**: 87–96.
[18] Zhang W, Su L, Lu D, *et al.* Resilient Si_3N_4@SiO_2 nanowire aerogels for high-temperature electromagnetic wave transparency and thermal insulation. *J Adv Ceram* 2023, **12**: 2112–2122.
[19] Yousufi MM, bin Dzulkarnain I, Elhaj MEM, *et al.* A perspective on the prospect of pickering emulsion in reservoir conformance control with insight into the influential parameters and characterization techniques. *Processes* 2023, **11**: 2672.
[20] Sepulveda P, Binner JGP. Processing of cellular ceramics by foaming and *in situ* polymerisation of organic monomers. *J Eur Ceram Soc* 1999, **19**: 2059–2066.
[21] Hammel EC, Ighodaro OLR, Okoli OI. Processing and properties of advanced porous ceramics: An application based review. *Ceram Int* 2014, **40**: 15351–15370.
[22] Studart AR, Gonzenbach UT, Tervoort E, *et al.* Processing routes to macroporous ceramics: A review. *J Am Ceram Soc* 2006, **89**: 1771–1789.
[23] Wang LY, An LQ, Zhao J, *et al.* High-strength porous alumina ceramics prepared from stable wet foams. *J Adv Ceram* 2021, **10**: 852–859.
[24] Chen Y, Wang NN, Ola O, *et al.* Porous ceramics: Light in weight but heavy in energy and environment technologies. *Mater Sci Eng R Rep* 2021, **143**: 100589.
[25] Deville S. Freeze-casting of porous ceramics: A review of current achievements and issues. *Adv Eng Mater* 2008, **10**: 155–169.
[26] Shao GF, Hanaor DAH, Shen XD, *et al.* Freeze casting: From low-dimensional building blocks to aligned porous structures—A review of novel materials, methods, and applications. *Adv Mater* 2020, **32**: e1907176.
[27] Qian L, Zhang HF. Controlled freezing and freeze drying: A versatile route for porous and micro-/nano-structured materials. *J Chem Technol Biotechnol* 2011, **86**: 172–184.
[28] Fu Q, Rahaman MN, Dogan F, *et al.* Freeze casting of porous hydroxyapatite scaffolds. I. Processing and general microstructure. *J Biomed Mater Res* 2008, **86B**: 125–135.
[29] Hou ZP, Ye F, Liu LM, *et al.* Fabrication of gradient porous β-SiAlON ceramics *via* a camphene-based freeze casting process. *Mater Sci Eng A* 2012, **558**: 742–746.
[30] Chen RF, Wang CA, Huang Y, *et al.* Ceramics with special porous structures fabricated by freeze-gelcasting: Using tert-butyl alcohol as a template. *J Am Ceram Soc* 2007, **90**: 3478–3484.
[31] Tang YF, Qiu S, Wu C, *et al.* Freeze cast fabrication of porous ceramics using tert-butyl alcohol–water crystals as template. *J Eur Ceram Soc* 2016, **36**: 1513–1518.
[32] Rosenau T, Potthast A, Hell J. *Cellulose Science and Technology: Chemistry, Analysis, and Applications*. John Wiley & Sons, 2018.
[33] Lu X, Arduini-Schuster MC, Kuhn J, *et al.* Thermal conductivity of monolithic organic aerogels. *Science* 1992, **255**: 971–972.
[34] Lucchini E, Maschio S. Thermal shock resistance of cordieritic filter for diesel engines. *Mater Sci Technol* 1995, **11**: 605–610.
[35] Alamo J, Roy R. Ultralow-expansion ceramics in the system Na_2O–$ZrO_2P_2O_5$–SiO_2. *J Am Ceram Soc* 1984, **67**: C78.
[36] Ayyar A, Chawla N. Microstructure-based modeling of crack growth in particle reinforced composites. *Compos Sci Technol* 2006, **66**: 1980–1994.
[37] Asl MS, Kakroudi MG, Noori S. Hardness and toughness of hot pressed ZrB_2–SiC composites consolidated under relatively low pressure. *J Alloys Compd* 2015, **619**: 481–487.
[38] Zhang DJ, Li YF, Lu HJ, *et al.* Influence of conversion on dielectric constant of dicyandiamide cured epoxy resin: A molecular dynamic simulation and experiment study. *Polymer* 2023, **267**: 125645.
[39] Martinez-Vega J. *Dielectric Materials for Electrical Engineering*. John Wiley & Sons, 2013.
[40] Cava RJ. Dielectric materials for applications in microwave communications. *J Mater Chem* 2001, **11**: 54–62.
[41] Ramirez C, Figueiredo FM, Miranzo P, *et al.* Graphene nanoplatelet/silicon nitride composites with high electrical conductivity. *Carbon* 2012, **50**: 3607–3615.
[42] Luo H, Tan YQ, Li Y, *et al.* Modeling for high-temperature dielectric behavior of multilayer C_f/Si_3N_4 composites in X-band. *J Eur Ceram Soc* 2017, **37**: 1961–1968.
[43] Chen F, Cao F, Pan HL, *et al.* Mechanical and dielectric properties of silicon nitride ceramics with high and hierarchical porosity. *Mater Des* 2012, **40**: 562–566.
[44] Yang HL, Li Y, Li QG, *et al.* Preparation and properties of porous silicon nitride ceramics with polymethyl methacrylate as pore-forming agent. *Ceram Int* 2020, **46**: 17122–17129.
[45] Fan BB, Li W, Zhang F, *et al.* Fabrication and properties of Si_2N_2O ceramics for microwave sintering furnace. *Process Appl Ceram* 2020, **14**: 32–39.
[46] Zhang T, Sun S, Cai JQ, *et al.* A new precursor to lightweight porous Si–Al–O–B ceramics with enhanced microwave transmissivity. *Ceram Int* 2020, **46**: 1974–1981.
[47] Li B, Liu K, Zhang CR, *et al.* Fabrication and properties of borazine derived boron nitride bonded porous silicon aluminum oxynitride wave-transparent composite. *J Eur Ceram Soc* 2014, **34**: 3591–3595.
[48] Wang SJ, Yang ZH, Duan ZM, *et al.* Fabrication and characterization of *in situ* porous Si_3N_4–Si_2N_2O–BN ceramic. *J Appl Ceram Tec* 2014, **11**: 832–838.
[49] Xia YF, Zeng YP, Jiang DL. Microstructure and mechanical properties of porous Si_3N_4 ceramics prepared by freeze-casting. *Mater Des* 2012, **33**: 98–103.
[50] Ye F, Zhang JY, Liu LM, *et al.* Effect of solid content on pore structure and mechanical properties of porous silicon nitride ceramics produced by freeze casting. *Mater Sci Eng A* 2011, **528**: 1421–1424.
[51] Zhang RB, Fang DN, Pei YM, *et al.* Microstructure, mechanical and dielectric properties of highly porous silicon nitride ceramics produced by a new water-based freeze casting. *Ceram Int* 2012, **38**: 4373–4377.